

RESEARCH ARTICLE

Four-dimensional computed tomography of the left ventricle, Part II: Estimation of mechanical activation times

Ashish Manohar¹ | Jed D. Pack² | Andrew J. Schluchter³ | Elliot R. McVeigh^{3,4,5}

¹Department of Mechanical and Aerospace Engineering, UC San Diego School of Engineering, La Jolla, California, USA

²Radiation Systems Lab, GE Global Research, Niskayuna, New York, USA

³Department of Bioengineering, UC San Diego School of Engineering, La Jolla, California, USA

⁴Department of Radiology, University of California San Diego, La Jolla, California, USA

⁵Department of Medicine, Cardiovascular Division, UC San Diego School of Medicine, La Jolla, California, USA

Correspondence

Elliot McVeigh, PhD, 9452 Medical Center Drive, La Jolla, CA 92037, USA.
Email: emcveigh@ucsd.edu

Funding information

American Heart Association, Grant/Award Number: AHA 20PRE35210261; National Heart, Lung, and Blood Institute, Grant/Award Number: R01HL144678

Abstract

Purpose: We demonstrate the viability of a four-dimensional X-ray computed tomography (4DCT) imaging system to accurately and precisely estimate mechanical activation times of left ventricular (LV) wall motion. Accurate and reproducible timing estimates of LV wall motion may be beneficial in the successful planning and management of cardiac resynchronization therapy (CRT).

Methods: We developed an anthropomorphically accurate in silico LV phantom based on human CT images with programmed septal-lateral wall dyssynchrony. Twenty-six temporal phases of the in silico phantom were used to sample the cardiac cycle of 1 s. For each of the 26 phases, 1 cm thick axial slabs emulating axial CT image volumes were extracted, 3D printed, and imaged using a commercially available CT scanner. A continuous dynamic sinogram was synthesized by blending sinograms from these static phases; the synthesized sinogram emulated the sinogram that would be acquired under true continuous phantom motion. Using the synthesized dynamic sinogram, images were reconstructed at 70 ms intervals spanning the full cardiac cycle; these images exhibited expected motion artifact characteristics seen in images reconstructed from real dynamic data. The motion corrupted images were then processed with a novel motion correction algorithm (ResyncCT) to yield motion corrected images. Five pairs of motion uncorrected and motion corrected images were generated, each corresponding to a different starting gantry angle (0 to 180 degrees in 45 degree increments). Two line profiles perpendicular to the endocardial surface were used to sample local myocardial motion trajectories at the septum and the lateral wall. The mechanical activation time of wall motion was defined as the time at which the endocardial boundary crossed a fixed position defined on either of the two line profiles while moving toward the center of the LV during systolic contraction. The mechanical activation times of these myocardial trajectories estimated from the motion uncorrected and the motion corrected images were then compared with those derived from the static images of the 3D printed phantoms (ground truth). The precision of the timing estimates was obtained from the five different starting gantry angle simulations.

Results: The range of estimated mechanical activation times observed across all starting gantry angles was significantly larger for the motion uncorrected images than for the motion corrected images (lateral wall: 58 ± 15 ms vs 12 ± 4 ms, $p < 0.005$; septal wall: 61 ± 13 ms vs 13 ± 9 ms, $p < 0.005$).

Conclusions: 4DCT images processed with the ResyncCT motion correction algorithm yield estimates of mechanical activation times of LV wall motion with significantly improved accuracy and precision. The promising results reported in this study highlight the potential utility of 4DCT in estimating the timing of mechanical events of interest for CRT guidance.

KEYWORDS

cardiac CT, cardiac mechanical activation time, cardiac resynchronization therapy, dyssynchronous left ventricular phantom, motion correction

1 | INTRODUCTION

Recent advances in four-dimensional X-ray computed tomography (4DCT) technology have permitted the functional imaging of a full cardiac cycle over the entire heart within a single heartbeat acquisition and from a single table position.^{1–3} Modern 4DCT imaging systems also produce images with high spatial resolution,⁴ allowing the visualization and tracking of the fine endocardial features comprising the trabeculae carneae and the papillary muscles.^{5,6} One important application for these images is predicting response to cardiac resynchronization therapy (CRT), which is a medical procedure for treating heart failure patients with mechanical dyssynchrony of the left ventricle. For many patients, this treatment is highly effective; unfortunately, the treatment response rate is currently a serious limitation, with 30–50% of patients not receiving much benefit as a result of their CRT procedure.⁷ A great deal of research has been done into how to use echocardiography or MR imaging to guide treatment decisions, but such efforts have not produced a robust solution due to poor performance from echo^{8,9} and the complexity and limited applicability of MR techniques (e.g., 28% of CRT candidates already have RV pacing in place, which limits the use of MR¹⁰).

In addition, recent studies have determined the benefits of 4DCT in estimating mechanical dyssynchrony and guiding optimal lead placement. Hoffmann and colleagues demonstrated the utility of multidetector CT systems to identify differences in the extent of left ventricular (LV) dyssynchrony between patients with heart failure and age-matched controls.¹¹ More recently, they determined the ability to predict 2-year major adverse cardiac events (MACEs) using dual-source CT. They also showed that leads placed on sites with maximal wall thickness were associated with fewer MACEs ($p < 0.01$).¹² Behar et al. used CT to determine the epicardial vein for targeting optimal lead placement.¹³ A CT-derived endocardial strain metric called SQUEEZ⁵ was used to identify regions of scar tissue and regions of latest mechanical activation. They reported that pacing at a site determined optimal by CT-SQUEEZ correlated with higher clinical response rates than those paced in nonoptimal regions (90% vs 60%).

However, previous studies have not addressed a major limitation in measuring temporal events with CT: the “false dyssynchrony” artifact.¹⁴ The temporal resolution of 4DCT is complex; motion artifacts seen in reconstructed CT images are due to the combined effect of gantry position as a function of time and the relative direction of wall motion.^{15,16} Edge locations in reconstructed CT images are updated every time the X-ray beam is tangent to the particular edge; therefore, depending on their orientation, different edges are updated at different points in time in a continuous 4DCT movie, giving the false impression of dyssynchronous contraction (Section 2.5 provides further insight into

the source of the false dyssynchrony artifact). These artifacts are usually not crucial in the assessment of global LV function; however, they impede the ability to accurately and precisely measure mechanical activation times at different locations on the LV wall. The accurate evaluation of activation times of wall motion and LV dyssynchrony provides critical information in the optimal planning and management of CRT.^{17,18}

Thus, the objective of this study was to perform the first quantitative evaluation of the accuracy and precision of estimating mechanical activation times^{19,20} of LV wall motion using 4DCT. To serve as ground truth, we developed an anthropomorphically accurate in silico LV phantom with programmable dyssynchrony. Twenty-six phases of the dyssynchronous LV in silico phantom were selected to sample the full simulated cardiac cycle of 1 s. For each of the 26 phases, fixed axial slabs of 1 cm in thickness were extracted, 3D printed, and imaged using a commercially available CT scanner (GE Revolution CT™). From these 26 static images of the 3D printed phantom, a continuous dynamic sinogram was synthesized, and images were reconstructed at 70 ms intervals spanning the full cardiac cycle. The images reconstructed from the synthetic sinogram exhibited the expected motion artifact characteristics seen in images reconstructed from true dynamic data. Five sets of images, each with a different starting gantry angle with respect to the heart cycle, were reconstructed, and the images were processed with a novel motion correction algorithm. Local myocardial trajectories measured from the motion corrected and the motion uncorrected images were compared with those measured in the ground-truth static images. Based on these trajectories, guidance for estimating the mechanical activation times of LV wall motion was obtained from this study.

2 | METHODS

2.1 | Dyssynchronous LV phantom development

2.1.1 | Image acquisition, image segmentation, and mesh extraction

A CT image of the end diastolic phase of a human LV was used as the baseline for phantom development. The image was acquired using a 256 detector row (Revolution CT™, General Electric Healthcare, Chicago, IL) scanner at the University of California San Diego using retrospective electrocardiogram gating with inspiratory breath hold. The subject (age: 45 years; sex: female) was scanned for one complete cardiac cycle (tube current: 148 mA; kVp: 80 kV), and the end diastolic phase was reconstructed at 0% of the R-R phase into a $512 \times 512 \times 256$ grid. The image had a pixel spacing of 0.41 mm in the x - y plane and a slice thickness of

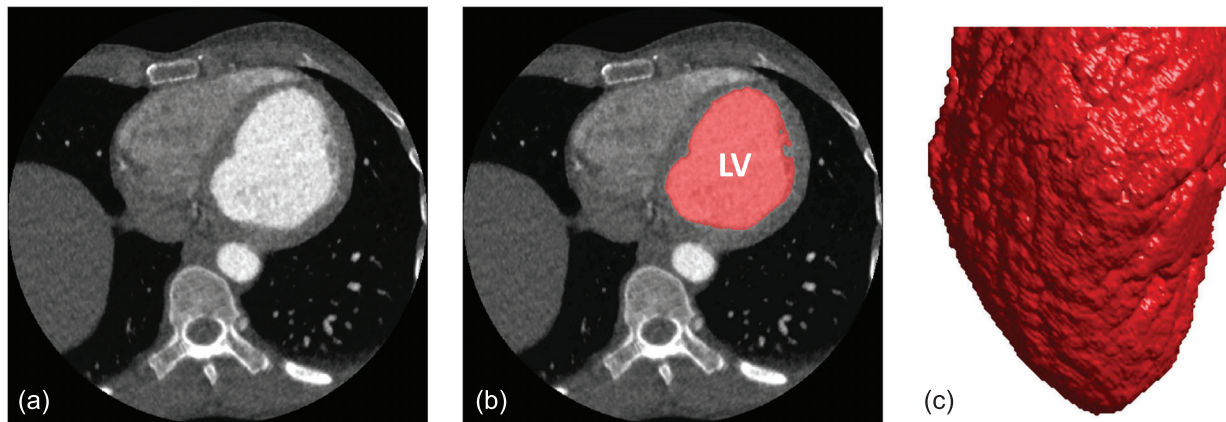


FIGURE 1 Image segmentation and mesh extraction. (a) Axial slice of the CT image. (b) Axial slice with the LV blood volume segmentation overlaid in red. (c) 3D rendering of the extracted LV endocardial mesh, looking at the lateral wall with the anterior wall to the left and the inferior wall to the right

0.625 mm in z . The reconstruction field of view diameter was 209 mm, and the “Standard” reconstruction kernel (name of the kernel on the GE Revolution CT™ scanner) was used. Neither subject enrollment, image acquisition, nor image reconstruction was performed for the purpose of this particular study; the subject was scanned, and images were acquired and reconstructed as per standard clinical protocols established at the center. The images of the subject were retrospectively used in this study in accordance with an IRB-approved protocol.

A mesh defining the LV endocardium was extracted in a manner similar to that described by Manohar et al.²¹ First, the end diastolic phase of the LV was segmented using the active contour region growing module in ITK-SNAP v3.6.2²² (thresholding type = high pass; threshold = 360 Hounsfield units (HU); smoothness = 10; seed radius = 10; all other parameters were set as default). The segmentation was then imported into MATLAB (MathWorks Inc.) and resampled to an isotropic resolution of 0.5 mm in x , y , and z dimensions. Finally, a mesh was extracted from the resampled segmentation using the *isosurface* built-in MATLAB routine, which comprised 98 911 faces and 49 627 mesh points. Figure 1 illustrates the process outlined above.

2.1.2 | Displacement functions

Dyssynchrony was programmed into the in silico LV phantom by prescribing displacements to the mesh points that were extracted as outlined above in Section 2.1.1. These displacements were designed to achieve the desired endocardial strains as a function of both endocardial location and time across the cardiac cycle. Two strains were simulated: longitudinal strain (ϵ_{ll}) as a function of only time (t) across the cardiac cycle and circumferential strain (ϵ_{cc}) as a function of both time (t) and endocardial azimuthal location (θ). The strain

functions used in this study were modeled based on realistic in vivo strains reported by Helm et al.²³ and Delgado et al.²⁴ and those derived from computer simulations using the CircAdapt model.²⁵

A time-dependent gradient in circumferential strain in the azimuthal direction (θ) was programmed to simulate an activation delay in contraction between the in silico phantom’s septal ($\theta = \pi$) and lateral walls ($\theta = 0$); this was done to emulate the activation delay that is clinically observed in patients with a left bundle branch block (LBBB) or right ventricular (RV) apical pacing.^{23,24} This gradient was achieved by defining one strain versus time curve for the lateral wall at $\theta = 0$ ($\epsilon_{CC_{lateral}}$) and another strain versus time curve for the septum at $\theta = \pi$ ($\epsilon_{CC_{septal}}$); the circumferential strain at all other endocardial locations $0 < |\theta| < \pi$ was a linearly interpolated value between the two defined strains at $\theta = 0$ and $\theta = \pi$. Figure 2a shows the designed longitudinal (solid blue) and circumferential (dashed red: lateral wall; dotted green: septum) strains as a function of time across the cardiac cycle. The R–R interval of the simulated cardiac cycle was set to 1 s.

The displacement functions were prescribed to the LV mesh points in the “cardiac frame of reference,” which was defined as the coordinate system in which the LV long axis was parallel to the z -axis (Figure 2b). The mesh points were transformed from a Cartesian coordinate system (x, y, z) to a cylindrical coordinate system (r, θ, z), with the origin set to the LV mesh centroid. Displacements were then prescribed to the mesh points (r, θ, z) according to the following equations:

$$r(\theta, t) = r(\theta, 0) * (1 + \epsilon_{cc}(\theta, t)), \quad (1)$$

$$z(t) = z_o + (z(0) - z_o) * (1 + \epsilon_{ll}(t)), \quad (2)$$

where t is time across the cardiac cycle, $t = 0$ represents end diastole, z_o is the fixed apical z coordinate of the LV

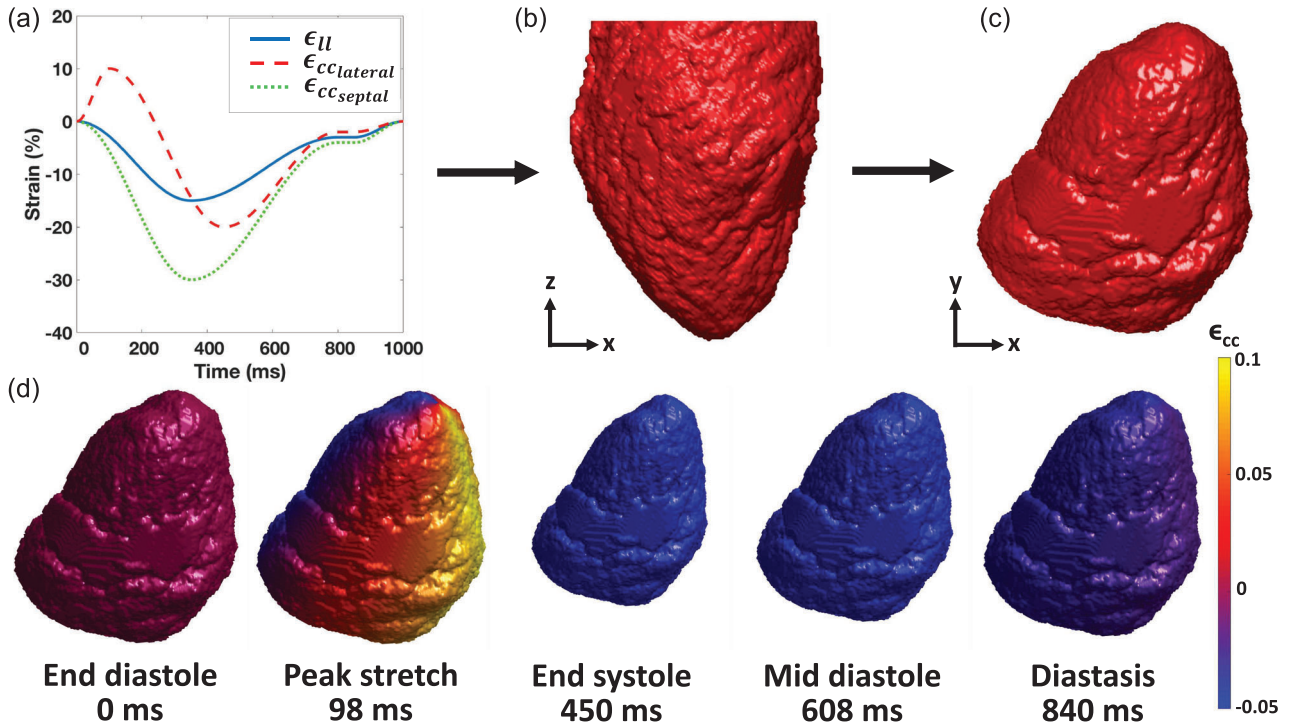


FIGURE 2 Simulation of LV dyssynchrony. (a) Longitudinal (ϵ_{ll} – solid blue) and circumferential ($\epsilon_{cc_{lateral}}$ – dashed red; $\epsilon_{cc_{septal}}$ – dotted green) strain curves as a function of time across the cardiac cycle. The R-R interval of the simulated cardiac cycle was set to 1 s. (b) 3D rendering of the end diastolic LV mesh in the cardiac frame of reference with the LV long axis parallel to the z-axis. The lateral wall is in view with the anterior wall to the left and the inferior wall to the right. (c) 3D rendering of the end diastolic LV mesh rotated back to its original orientation in the scanner frame of reference. The inferior wall is in view with the septum on the left and the lateral wall on the right, looking from the patient’s feet up toward the head. (d) 3D renderings of the analytically deformed meshes of the dyssynchronous LV in silico phantom at five phases of the cardiac cycle with regional circumferential strain values mapped onto the endocardial surface. Blue represents endocardial contraction, and yellow represents endocardial stretch. The orientation of the LV is the same as in Figure 2c

mesh, and $\epsilon_{cc}(\theta, t)$ is the circumferential strain at time t for a point with an azimuthal coordinate of $0 \leq |\theta| \leq \pi$, given by the equation:

$$\epsilon_{cc}(\theta, t) = \left(\epsilon_{cc_{septal}}(t) - \epsilon_{cc_{lateral}}(t) \right) * \frac{|\theta|}{\pi} + \epsilon_{cc_{lateral}}(t), \quad (3)$$

After prescribing the displacement functions, the mesh points (r, θ, z) were transformed back to the Cartesian coordinate system (x, y, z) . The LV mesh was then rotated back to its original orientation in the scanner frame of reference, as shown in Figure 2c. Figure 2d shows analytically deformed meshes of the in silico phantom at five phases of the cardiac cycle with regional ϵ_{cc} values mapped onto the endocardial surface (blue represents contraction, and yellow represents stretch).

2.2 | 3D printing and CT imaging of the dyssynchronous LV phantom

Twenty-six phases of the dyssynchronous LV in silico phantom were chosen to sample the simulated cardiac cycle of 1 s. The first phase was at 0 ms, and the 26th

phase was at 975 ms of the simulated cardiac cycle. The 26 phases were chosen with variable time intervals such that no single mesh point had more than 2 mm displacement between any two consecutive phases. These 26 phases were sufficient to sample the programmed motion of the phantom across the simulated cardiac cycle, as shown in Figures S1 and S2.

2.2.1 | Generation of axial slabs and 3D printing

Axial slabs of 1 cm in thickness fixed in the scanner z-direction were extracted from each of the 26 phases of the dyssynchronous LV in silico phantom (Figure 3a). The fixed axial slabs emulated clinical axial CT image volumes with the phantom’s tissue moving in and out of the axial plane as it was programmed to contract and relax. The particular slab shown in Figure 3a was chosen because it sampled both the delayed contracting lateral wall and the earlier contracting septum. These in silico axial slabs were 3D printed to create physical phantoms. Each physical phantom, representing a particular phase of the cardiac cycle, was printed in the shape of a cylinder with a hollow LV cavity in the

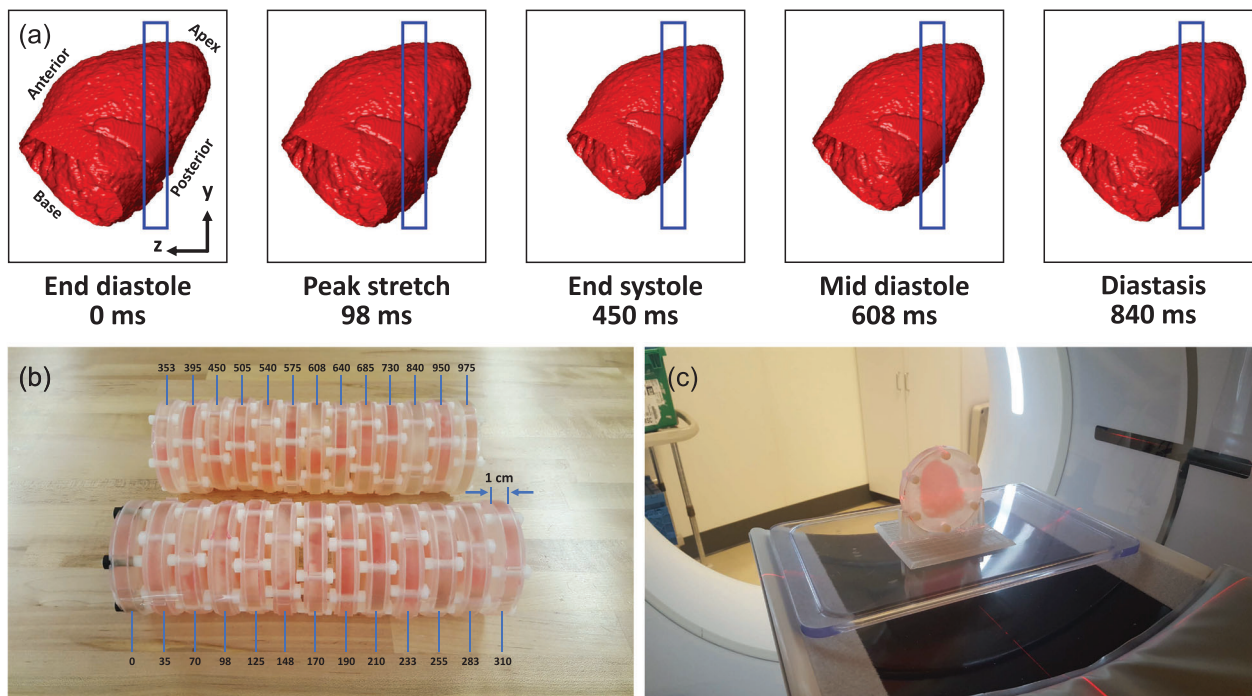


FIGURE 3 3D printing and CT imaging of the 1 cm thick axial slabs of the dyssynchronous LV phantom. (a) Right sagittal views of the meshes of the dyssynchronous LV in silico phantom at five phases of the cardiac cycle. The blue rectangle shows the 1 cm axial slab fixed in space; for each phase of the cardiac cycle, mesh points within that slab were extracted. (b) Stack of the 26 3D printed 1 cm thick cylinders of the dyssynchronous LV phantom. Each 3D printed phantom cylinder represents a particular phase of the cardiac cycle and is labeled with its corresponding time delay in milliseconds after end diastole. (c) The 98 ms phantom cylinder positioned in the CT scanner for imaging. The phantom was locked into position using a holder fixed onto the scanner table

center using a *Form 3* stereolithography printer (Formlabs Inc., Somerville, MA). The printing material used was a proprietary clear photopolymer resin (FLGPCL04), and the central LV cavity was filled with an iodinated nonionic radiocontrast agent (10% by volume solution of Visipaque™ 320, General Electric Healthcare, Chicago, IL). Figure 3b shows the 26 3D printed phantom cylinders labeled with their corresponding time delays in milliseconds after end diastole. Figure 3c shows the positioning holder and an example 3D printed phantom (corresponding to the 98 ms phase) positioned in the CT scanner; tabs on the side of each phantom locked each phantom into position to maintain spatial alignment over the time frames.

2.2.2 | CT imaging

A 256 detector row (Revolution CT™, General Electric Healthcare, Chicago, IL) clinical CT scanner was used to image the 26 3D printed phantom cylinders. Each cylinder was imaged for a total of 450 ms under 100 kVp, 350 mA, and small focal spot tube settings. The raw data for each scan were saved using the standard archiving software on the scanner. Each image was reconstructed into a $512 \times 512 \times 128$ grid with pixel

spacing of 0.49 mm in the x - y plane and a slice thickness of 0.625 mm in z . The “Standard” reconstruction kernel (name of the kernel on the GE Revolution CT™ scanner) was used with a reconstruction field of view diameter of 250 mm. The HU values of the photopolymer resin and the contrast solution were 120 ± 15 and 1065 ± 30 , respectively. These images, referred to hereafter as the “static” images, served as the motion artifact-free ground-truth images of the dyssynchronous LV phantom, sampling the simulated cardiac cycle in 26 phases from 0 to 975 ms. Figure 4 shows the CT reconstructed images of the 3D printed phantom cylinders at five phases of the cardiac cycle.

2.3 | Dynamic raw data synthesis and image reconstruction

The raw data for each of the 26 images acquired as described above were saved using the standard archiving software on the scanner. These individual raw datasets, each representing a static phase of the 3D printed phantom, were first converted to sinograms that can be reconstructed (data prep). The prepped sinograms were then used to create a synthetic dynamic sinogram that emulated the sinogram that would be

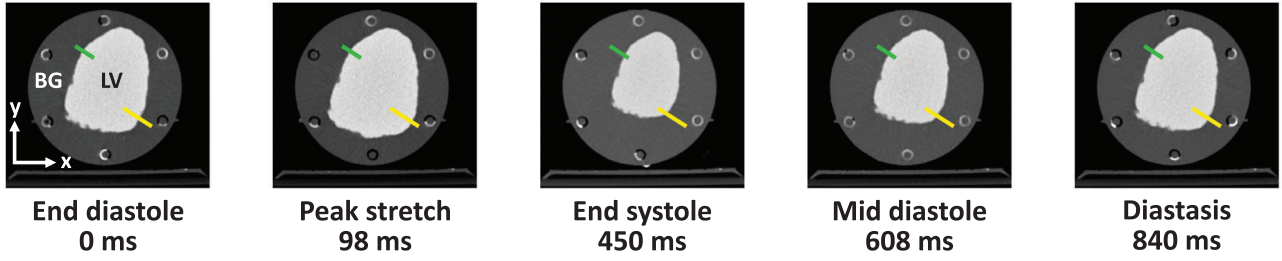


FIGURE 4 CT reconstructed images of the 3D printed phantom cylinders at five phases of the cardiac cycle. The circular gray background is the photopolymer resin (printing material). The LV cavity is filled with an iodinated radiocontrast solution. The green and yellow lines represent the septal wall and the lateral wall m-mode sampling lines, respectively. LV: left ventricle; BG: background resin

acquired if the dyssynchronous phantom contracted and relaxed continuously in real time.

The first step in the synthesis of the dynamic sinogram was the extraction of a single full scan view range (360 degrees) from each prepped static sinogram. The views were then circularly shifted to align the starting view angles. To ensure that there was no discontinuity at the wrap around point, the extracted view range was initially larger than one rotation, and a gradual linear blending function was employed to combine the earliest and latest views.

Given a reference view angle (β_c) and a corresponding reference time (t_c), one can compute the view angle positions that correspond exactly to each static phase (for each of multiple cardiac cycles) as follows:

$$\beta_{n+26N} = \beta_c + (t_n - t_c + 1000N) \cdot \omega, \quad (4)$$

where N is an integer that indexes the cardiac cycle (e.g., -1 for the previous cardiac cycle, 0 for the current cycle, 1 for the next cardiac cycle), n is an integer from 1 to 26 indicating the phase index, and ω is the gantry rotation speed in radians per millisecond. A dynamic sinogram (D_{β_c, t_c}) was then computed from the static sinograms (S_i) using linear interpolation at each view angle based on the two nearest phases, as follows:

$$D_{\beta_c, t_c}(\beta, \gamma, \alpha) = (1 - w(\beta)) \cdot \hat{S}_{i(\beta)}(\hat{\beta}, \gamma, \alpha) + w(\beta) \cdot \hat{S}_{i(\beta)+1}(\hat{\beta}, \gamma, \alpha), \quad (5)$$

where β is the view angle, γ is the fan angle, α is the cone angle, and $w(\beta)$ is a linear interpolation weight in the range $[0, 1]$, given by the following equation:

$$w(\beta) = \frac{\beta - \beta_{i(\beta)}}{\beta_{i(\beta)+1} - \beta_{i(\beta)}}, \quad (6)$$

and $i(\beta)$ is defined as the unique index i such that

$$\beta_i \leq \beta < \beta_{i+1}, \quad (7)$$

Additionally, \hat{S}_i and $\hat{\beta}$ are defined via the modulo operator as follows:

$$\hat{S}_i(\beta, \gamma, \alpha) = S_{i \bmod 26}(\beta, \gamma, \alpha), \quad (8)$$

$$\hat{\beta} = \beta \bmod 2\pi, \quad (9)$$

To provide a multiphase reconstruction series that covered the entire heart cycle (and to be able to apply our motion correction algorithm), we generated dynamic sinograms that covered a time period slightly larger than one heart cycle. Reconstructions were performed using scanner reconstruction software (GE Revolution CT™) at 90-degree intervals (70 ms intervals for a gantry rotation speed of 280 ms), yielding 14 phases that sampled the full cardiac cycle from 0 to 980 ms. The resulting images clearly manifested the expected motion artifact characteristics seen in images reconstructed from real dynamic data, including “double-wall” and “stationary-wall” artifacts and distortions that rotate in concert with the orientation of the gantry angle.²⁶ Intra window motion is included in the linear interpolation of sinogram data during synthetic sinogram creation. The difference between the continuous sinogram and the interpolated sinogram yields artifacts in the reconstructed images that are imperceptible compared with the larger “double-wall” and “stationary-wall” artifacts²⁷; these larger artifacts are the primary sources of error in the estimation of mechanical activation times of wall motion.

The motion-corrupted images, referred to hereafter as the “uncorrected” images, were then processed with a novel motion correction algorithm called ResyncCT²⁶ to produce motion corrected images at the same 14 phases of the cardiac cycle as that of the uncorrected images. ResyncCT is a new cardiac CT motion correction algorithm that leverages the power of conjugate pairs of partial angle reconstruction images for motion estimation and motion compensation. The motion corrected images are referred to hereafter as the “ResyncCT” images. This entire process was repeated for five different starting gantry angles by using a

reference time of zero ($t_c = 0$) and reference view angles of:

$$\beta_c(k) = k \cdot \frac{\pi}{4}, \quad (10)$$

where k is an integer from 0 to 4, representing the five different starting gantry angles (0, 45, 90, 135, and 180 degrees).

2.4 | M-mode imaging

The effect of CT motion artifacts on the estimate of the position of the endocardium was quantified by sampling endocardial wall positions as a function of time across the cardiac cycle in a manner similar to ultrasound m-mode imaging.^{28,29} The lateral wall m-mode line (shown by the yellow line in Figure 4) was placed close to the site of programmed latest activation. The septal wall m-mode line (shown by the green line in Figure 4) was placed at a point of earlier activation on the septum.

Endocardial wall positions as a function of time were sampled along the m-mode lines for each of the static, uncorrected, and ResyncCT images. These m-mode images were then upsampled via cubic interpolation by a factor of 10 to achieve subpixel resolution, thereby reducing the effects of pixel discretization. The endocardial boundary (edge) was detected from each m-mode image by applying a threshold of 530 HU, which was the optimal threshold for LV blood volume segmentation as determined by Otsu's method.³⁰

The first three rows of Figure 5a–c show the uncorrected images sampled at three phases of the cardiac cycle; the full set of reconstructions (not shown) span the cardiac cycle from 0 to 980 ms in 70 ms intervals. Each column corresponds to a simulated starting gantry angle: 0°, 45°, 90°, 135°, and 180° from left to right. Figure 5d shows the lateral wall m-mode images sampled at the endocardial wall location shown by the yellow line. In Figure 5a–c, the semicircle represents the trajectory of the X-ray source (white object) as it rotates in the counterclockwise direction (for 0°, the source trajectory is centered at 12 o'clock; for 90°, the source is centered at 9 o'clock). The green part of the trajectory represents the new “updated” views used in the reconstruction of a particular time frame of the object, assuming an image is reconstructed every 70 ms (with a 280 ms gantry rotation time). The red part of the trajectory represents views used in the reconstruction of a time frame of the object that are shared with its previous time frame. Hence, edges of the object parallel to the rays within the green views are updated in the new time frame, while edges parallel to the rays within the red views remain unchanged from the previous time

frame. This is the source of the false dyssynchrony artifact.^{14,26}

2.5 | Dynamics of endocardial boundary motion during systole

The septal and lateral wall m-mode images were used to investigate the artifacts in the measured dynamics of endocardial boundary motion during systole. The endocardial boundary was detected from each of the m-mode images derived from the static, uncorrected, and ResyncCT images. The uncorrected and ResyncCT images had endocardial boundaries sampled for five simulated starting gantry angles. The endocardial boundary positions derived from the static images served as the ground-truth for error estimation; these boundary positions were not dependent on the starting gantry angle.

For a predetermined “critical” position along the length of the m-mode line, the time at which the endocardial boundary crossed this position during systole was estimated. The critical position and the time at which the endocardial boundary crossed that position are referred to hereafter as the mechanical activation position (MAP) and the mechanical activation time (MAT), respectively. The motivation behind estimating this value was to assess the accuracy and precision of measuring mechanical activation times at local regions of the heart wall from 4DCT images, both with and without motion correction. MATs were estimated for all three classes of images: the static, uncorrected, and ResyncCT images. The MATs estimated from the uncorrected (T_U) and the ResyncCT (T_R) images were compared with those estimated from the static images (T_0 ; ground truth). Figure 6 illustrates an example estimation of the MATs (T_0 , T_U , and T_R) for a defined MAP (y_0) along the length of the lateral wall m-mode line. This process was repeated for a series of MAPs defined in intervals of 0.5 mm along the lengths of both the septal wall and the lateral wall m-mode lines. For the lateral wall, 11 positions between 9 and 14 mm were defined along the length of the m-mode line, while eight positions between 7 and 10.5 mm were defined for the septal wall m-mode line. These positions were chosen such that they sampled the full range of systolic endocardial boundary motion at both the lateral wall and the septal wall m-mode locations.

At each MAP, the range of estimated MATs observed over all gantry angles was calculated for both the uncorrected and the ResyncCT images. The distribution of ranges in MATs across all defined MAPs was then tested for statistically significant differences between the uncorrected and ResyncCT images using the two-sample t-test. A p value of < 0.05 was considered significant.

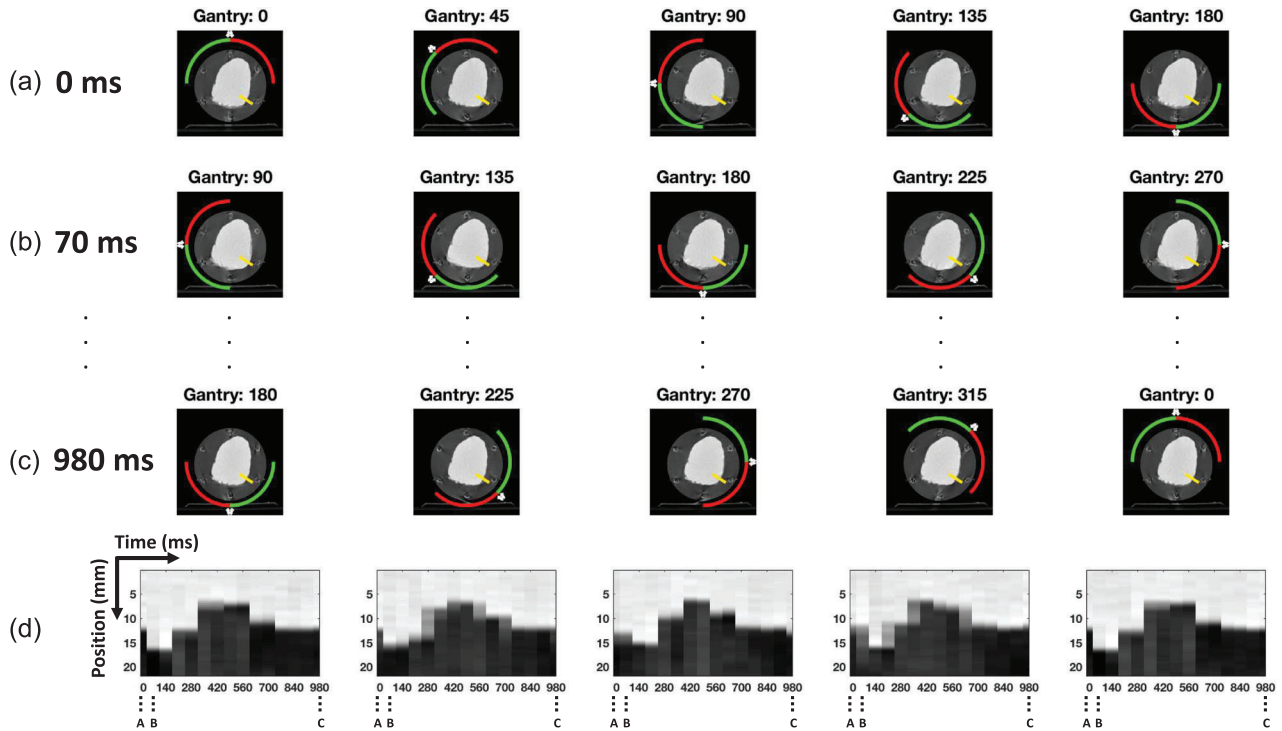


FIGURE 5 Simulated CT image acquisition, reconstruction, and m-mode imaging. Each column corresponds to a simulated starting gantry angle: 0°, 45°, 90°, 135°, and 180° from left to right, where the angular value of the source at the center of the acquisition is used to label each trajectory. The semicircles shown in rows A–C represent the trajectory of the X-ray source (white object) as it rotates in the counterclockwise direction from 0° at 12 o'clock to 180° at 6 o'clock. The green part of the trajectory represents new views acquired that are used in the reconstruction of a particular time frame of the object. The red part of the trajectory represents views used in the reconstruction of a time frame of the object that are shared with its previous time frame. (a–c) Reconstructions of the uncorrected images of the LV phantom at 3 of the 14 total phases of the cardiac cycle for a set of simulated starting gantry angles (columns). (d) Lateral wall m-mode images sampled at the endocardial lateral wall location shown by the yellow line. For each tile, the y-axis is the endocardial position along the length of the m-mode line in mm, and the x-axis is the time across the cardiac cycle in milliseconds; the motion of the wall is shown as the change in position of the boundary between the bright blood and the darker wall

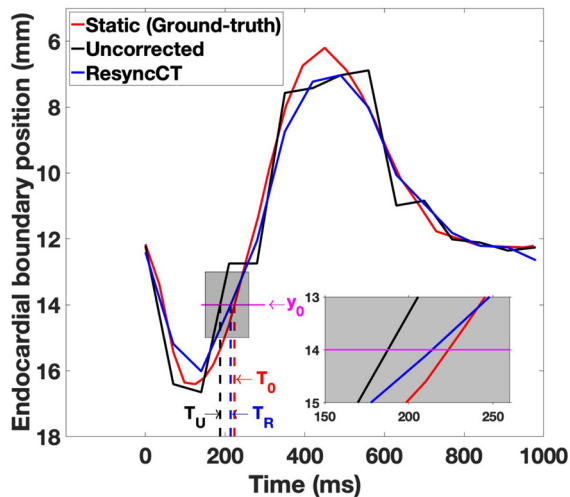


FIGURE 6 Estimation of mechanical activation times (MATs) at a defined mechanical activation position (MAP). For a defined MAP (y_0) along the length of the lateral wall m-mode line, the times at which the static (T_0 – ground truth; red), the uncorrected (T_U ; black), and the ResyncCT (T_R ; blue) derived endocardial boundaries crossed the MAP ($= y_0$) were estimated as their respective mechanical activation times (MAT)

2.6 | Time to maximal outward displacement

The programmed displacement functions made the lateral wall, at the location sampled by the lateral wall m-mode line, reach its maximum outward position at the 123 ms time point of the cardiac cycle; this was the ground-truth value of the time to maximal outward displacement (TMOD) of the late activated lateral wall. This time is a possible parameter for the characterization of mechanical activation delay and has been previously used in tagged magnetic resonance imaging (MRI) studies of dyssynchrony.^{19,20} The TMOD calculation was performed only for the lateral wall m-mode images.

The TMOD values of the lateral wall endocardial boundaries derived from the uncorrected and ResyncCT images were measured by fitting a second-degree polynomial to the first five time points (0, 70, 140, 210, 280 ms; Figure 7) of the endocardial boundary positions according to the model:

$$y = a_0 + a_1 t + a_2 t^2, \quad (11)$$

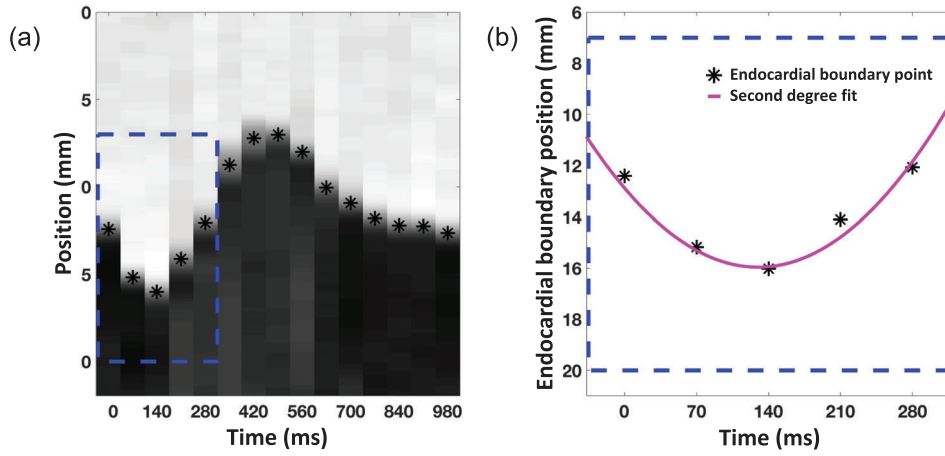


FIGURE 7 Estimation of the time to maximal outward displacement (TMOD). (a) Lateral wall m-mode image derived from the 0° starting gantry angle ResyncCT image. The dashed blue box is the highlighted region of interest shown in Figure 7b. The black asterisks correspond to the endocardial boundary positions. (b) Second degree polynomial fit (magenta) to the first five time points of the endocardial boundary positions used in the estimation of TMOD

where y is the position of the endocardial boundary in mm and t is time across the cardiac cycle in milliseconds. TMOD was then calculated as the extremum of the fitted function, given by the equation

$$TMOD = f(a_1, a_2) = \frac{-a_1}{2a_2} \quad (12)$$

The covariance matrix of the coefficients of the polynomial fit was estimated according to the following equation to obtain the confidence intervals of the fitted TMOD value:

$$Cov = \frac{(R^{-1} * R^{-1}') * normr^2}{df}, \quad (13)$$

where Cov is the covariance matrix, R is the triangular R factor from a QR decomposition of the Vandermonde matrix of the input query points, $normr$ is the norm of the residuals, and df is the number of degrees of freedom. The variance of the fitted TMOD value was then estimated according to the following equation:

$$Var[f(a_1, a_2)] = \sum_{i=1}^2 f'_i(a_1, a_2)^2 * Var[a_i] + 2 \sum_{i>j} f'_i(a_1, a_2) * f'_j(a_1, a_2) * Cov[a_i, a_j], \quad (14)$$

where Var is the variance. A TMOD value was estimated for each starting gantry angle simulation for both the uncorrected and the ResyncCT images, yielding a total of 10 TMOD values (five uncorrected and five ResyncCT).

The standard deviation ($\pm 1\sigma$) around each TMOD value was calculated as the square root of the variance derived from the polynomial fits. The distribu-

tion of ranges ($= 2\sigma$) in the TMOD estimates observed over all five starting gantry angles was then tested for statistically significant differences between the uncorrected and the ResyncCT images using the two-sample t-test. A p -value of < 0.05 was considered significant.

3 | RESULTS

3.1 | Septal wall and lateral wall m-mode images

Figure 8 shows the lateral wall m-mode images as a function of time across the cardiac cycle. Each column corresponds to a simulated starting gantry angle of 0° through 180° from left to right. The m-mode images were sampled at 70 ms regular intervals across the cardiac cycle from 0 to 980 ms. Figures 8a and 8c show the m-mode images derived from the uncorrected images, while Figures 8b and 8d show the m-mode images derived from the ResyncCT images. Figures 8a and 8b show the grayscale images, and Figures 8c and 8d show the binarized images after applying a threshold of 530 HU. The overlaid red dots correspond to the ground-truth endocardial boundary positions (derived from the static images) across the cardiac cycle sampled by the lateral wall m-mode line.

Similarly, Figure 9 shows the septal wall m-mode images as a function of time across the cardiac cycle for the five simulated starting gantry angles. Figures 9a and 9c show the m-mode images derived from the uncorrected images, and Figures 9b and 9d show the m-mode images derived from the ResyncCT images. Figures 9a–b show the grayscale images, and Figures 9c–d show the binarized images after applying a threshold of 530 HU. The overlaid red dots correspond to the ground-truth endocardial boundary

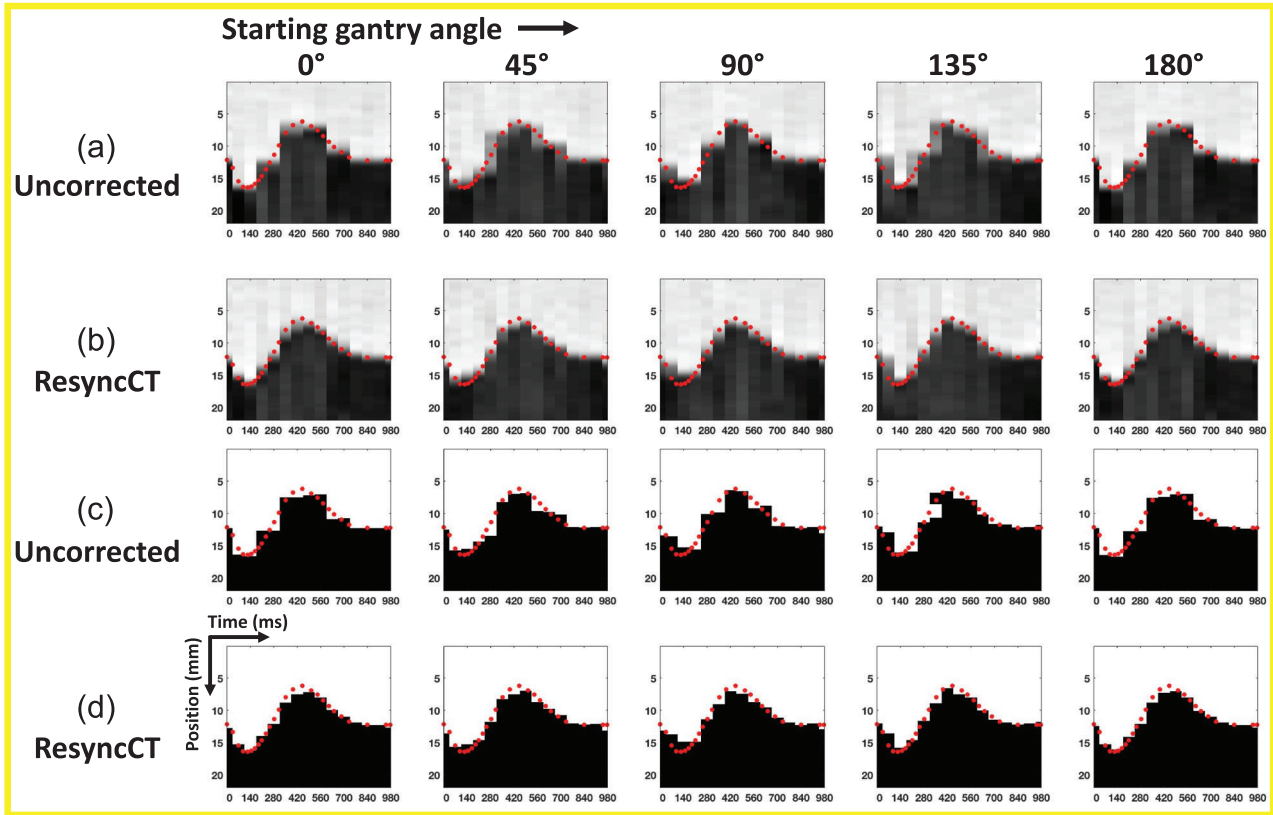


FIGURE 8 Lateral wall m-mode images of the endocardium as a function of time across the cardiac cycle for the five simulated starting gantry angles: 0° , 45° , 90° , 135° , and 180° . (a–b) Grayscale m-mode images derived from (a) the uncorrected and (b) the ResyncCT images. (c–d) Binarized m-mode images derived from (c) the uncorrected and (d) the ResyncCT images, showing the endocardial boundary positions as defined by the images. The red dots correspond to the ground-truth endocardial boundary positions across the cardiac cycle sampled by the lateral wall m-mode line from the static images. For each tile, the y-axis is position along the length of the m-mode line in mm, and the x-axis is time across the cardiac cycle in milliseconds

positions (derived from the static images) across the cardiac cycle sampled by the septal wall m-mode line.

It is clear from Figures 8 and 9 that the ground-truth endocardial boundary positions (red dots) are closer to the boundaries observed in the ResyncCT corrected images. This difference in accuracy is also summarized in Figure 10. It is also clear that the starting gantry angle has a significant effect on the positions of the endocardial boundary as a function of time across the cardiac cycle.

3.2 | Dynamics of endocardial boundary motion during systole

Figure 6 describes an example estimation of the MATs for a defined MAP along the length of the lateral wall m-mode line; the numerical values associated with Figure 6 are specified here. For a MAP of 14 mm (y_0), the MATs of the endocardial boundaries derived from the static, uncorrected, and ResyncCT images were $T_0 = 223$ ms (ground-truth), $T_U = 185$ ms, and $T_R = 207$ ms, respectively.

Figure 10 extends the data shown in Figure 6 to include all the defined MAPs and all five gantry angle simulations for both the septal and lateral wall m-mode lines. Figures 10a and 10c show the data for the lateral wall, while Figures 10b and 10d show the data for the septal wall. Figures 10a and 10b show the endocardial boundary positions across the cardiac cycle sampled by the m-mode lines for the five starting gantry angles. The boundaries derived from the static, uncorrected, and ResyncCT images are shown by the red, black, and blue lines, respectively. Figures 10c and 10d show the distributions of the MATs estimated from the uncorrected (gray boxes) and the ResyncCT (blue boxes) images as a function of the defined MAPs. Each distribution contains five points, corresponding to the five simulated starting gantry angles. The red lines correspond to the ground-truth MAT at each defined MAP, estimated from the static images.

The range of MATs observed across all five starting gantry angles and estimated over all MAPs was significantly higher for the uncorrected images than for the ResyncCT images (lateral wall: 58 ± 15 ms vs 12 ± 4 ms, $p < 0.005$; septal wall: 61 ± 13 ms vs 13 ± 9 ms, $p < 0.005$). From Figure 10, it is clear that the MATs

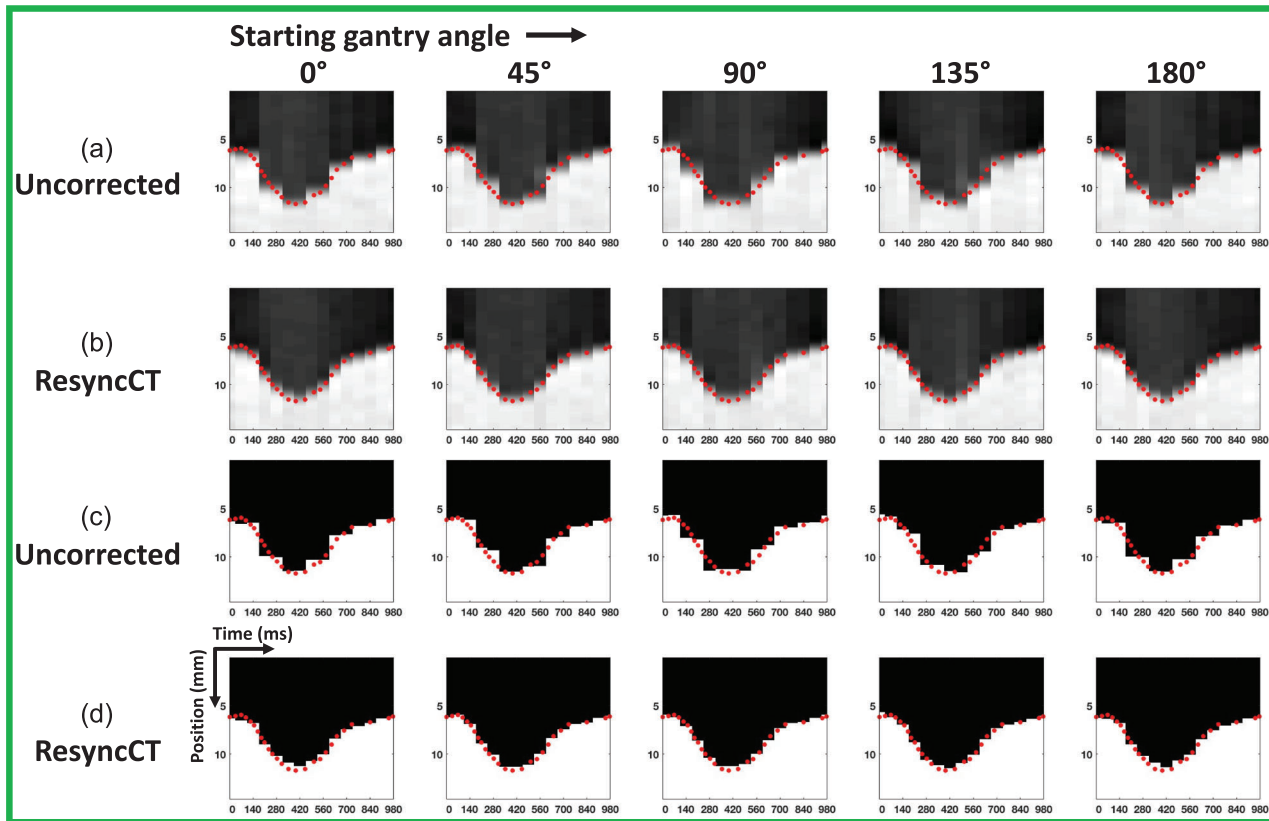


FIGURE 9 Septal wall m-mode images of the endocardium as a function of time across the cardiac cycle for the five simulated starting gantry angles: 0° , 45° , 90° , 135° , and 180° . (a–b) Grayscale m-mode images derived from (a) the uncorrected and (b) the ResyncCT images. (c–d) Binarized m-mode images derived from (c) the uncorrected and (d) the ResyncCT images, showing the endocardial boundary positions as defined by the images. The red dots correspond to the ground-truth endocardial boundary positions across the cardiac cycle sampled by the septal wall m-mode line from the static images. For each tile, the y-axis is position along the length of the m-mode line in mm, and the x-axis is time across the cardiac cycle in milliseconds

estimated from the ResyncCT images have a much lower error and much higher reproducibility with respect to different starting gantry angles than those estimated from the uncorrected images. It is also clear that the precision of the estimate is dependent on where the MAT is estimated with respect to the trajectory of the endocardial boundary motion during systole.

3.3 | Time to maximal outward displacement

Figures 11a and 11b show the second-degree polynomial fits (magenta) to the first five time points (0, 70, 140, 210, and 280 ms) of the endocardial boundary positions. These second-degree fits were used to estimate the TMOD of the endocardial wall location sampled by the lateral wall m-mode line. Each column corresponds to a simulated starting gantry angle of 0° through 180° from left to right. Figure 11a shows the estimation of TMOD for the endocardial boundaries derived from the uncorrected images, and Figure 11b shows the estimation of TMOD for the boundaries derived from the ResyncCT

images. Figure 11c shows the standard deviation ($\pm 1\sigma$) around the TMOD estimates for each of the five simulated starting gantry angles. The dashed red line corresponds to the ground-truth TMOD value of 123 ms. The range ($= 2\sigma$) of the TMOD estimates observed over all five simulated starting gantry angles was 41 ± 8 ms for the uncorrected images and 18 ± 7 ms for the ResyncCT images ($p < 0.005$). It should be noted that endocardial stretch is small or does not occur at all in some failing left ventricles; therefore, it is likely not a good parameter for measuring the timing of mechanics with 4DCT.

4 | DISCUSSION

The objective of this study was to develop an anthropomorphically accurate LV phantom with programmable dyssynchrony to test the efficacy of 4DCT in estimating the timing of cardiac mechanical events. The main findings of this study reveal that motion correction of 4DCT images significantly improves the accuracy and precision of estimating mechanical activation times of LV wall motion at local regions of the heart wall.

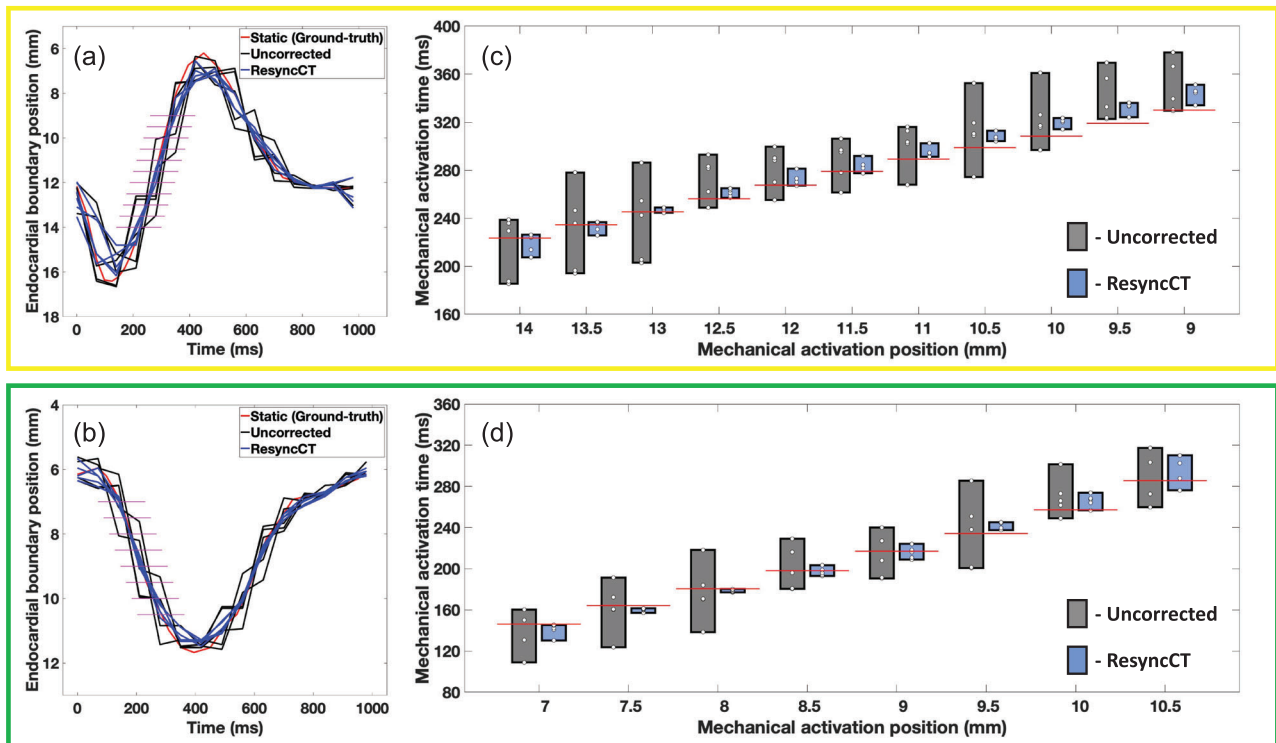


FIGURE 10 Dynamics of endocardial boundary motion during systole. (a–b) Endocardial boundary positions as a function of time across the cardiac cycle sampled by the (a) lateral wall m-mode and (b) septal wall m-mode. The endocardial boundary positions derived from the static, uncorrected, and ResyncCT images are shown by the red, black, and blue lines, respectively. (c–d) Distributions of mechanical activation times (MATs) as a function of defined mechanical activation positions (MAPs) estimated from the uncorrected (gray boxes) and the ResyncCT (blue boxes) images. The red lines represent the ground-truth MAT estimated from the static images. Each distribution contains five points corresponding to the five simulated starting gantry angles. The locations of the defined MAPs in relation to the trajectory of endocardial boundary motion are shown by the magenta lines in Figures 10a–b

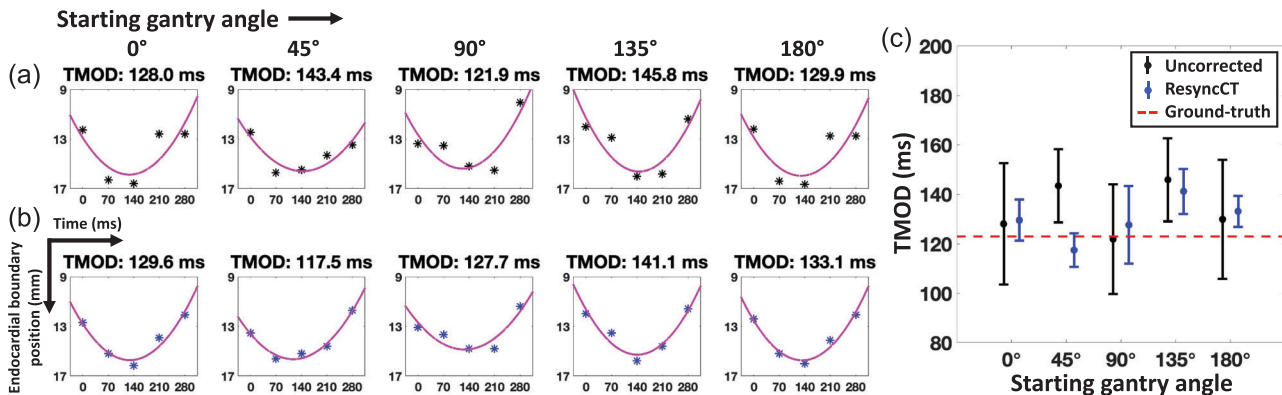


FIGURE 11 Time to maximal outward displacement (TMOD) of the endocardial wall location sampled by the lateral wall m-mode line. (a–b) Second degree polynomial fits (magenta) to the first five time points of the endocardial boundary positions derived from (a) the uncorrected (black asterisks) and (b) the ResyncCT (blue asterisks) images. Each column corresponds to a simulated starting gantry angle. (c) ± 1 standard deviation around the TMOD estimates derived from the uncorrected (black) and ResyncCT (blue) images for each of the five simulated starting gantry angles. The dashed red line corresponds to the ground-truth TMOD value of 123 ms

To the best of our knowledge, the phantom described in this paper is the first anthropomorphically accurate LV phantom to be used in the estimation of mechanical activation times of LV wall motion using 4DCT. The 4D XCAT phantom has previously been used as a

simulation tool in the assessment of mechanical LV dyssynchrony using gated SPECT MPI.³¹ Although not performed in this study, local regions of dysfunction simulating ischemic/scar tissue could be incorporated into the motion model of the dyssynchronous phantom;

this could be used to test the ability of 4DCT imaging systems to identify viable myocardium for optimal lead placement.

The temporal resolution of 4DCT is more complex than just reconstructing more time frames across the cardiac cycle with shorter time intervals in between the frames. The accuracy and precision of measuring mechanical activation times actually depends on the position of the gantry with respect to the direction of endocardial wall motion. For 4DCT cardiac imaging, each time frame is reconstructed from data acquired over $180^\circ + \text{fan angle}$ (“halfscan” reconstruction),¹⁵ and the reconstructed image is not a simple temporal average of the true image of the moving heart within this acquisition window. Instead, each spatial frequency component of the image has its own temporal skew, which is determined by the time at which the corresponding rays (orthogonal to its orientation) are measured during the acquisition. Since each spatial frequency has excellent “local” temporal resolution due to the submillisecond acquisition of each ray, motion compensation can be achieved if the temporal skew associated with each spatial frequency is accurately modeled.

The developed dyssynchronous LV phantom was used to assess the accuracy and precision of estimating mechanical activation times of LV wall motion at local regions of the endocardium using 4DCT, both with and without motion correction. Since there is no universally accepted definition nor method of computation of “mechanical activation time,”^{17,19,32} a series of “activation times” spanning the full range of endocardial systolic wall motion (MATs) was investigated, including the time to peak outward motion of the delayed contracting lateral wall (TMOD). Motion correcting the 4DCT images with the ResyncCT software yielded mechanical activation times of endocardial wall motion that were significantly more accurate and precise than those obtained from images without motion correction. Multiple studies have reported that the mechanical activation delays between segments of the LV wall are on the order of $\sim 120 \pm 100$ ms in patients with a left bundle branch block,^{33,34} whereas the delays in healthy controls are on the order of 20 ± 10 ms.³⁵ The MAT estimates obtained from the ResyncCT images have high precision, which can enable the detection of LV dyssynchrony using 4DCT with high confidence.

4DCT wide detector imaging systems have excellent spatial resolution, are easy to operate and permit rapid imaging of the heart (~ 160 ms per image). 4DCT is also available to those patients with implanted metallic medical devices. Additionally, with recent advances in CT technology, the average radiation dose from a cardiac function scan is < 3 mSv, which is less than the average dose received from natural sources in a year.³⁶ The ability to image within a single heartbeat eliminates step artifacts, which is a major limitation when

imaging patients with arrhythmia. These advantages coupled with the encouraging results from this study highlight the potential utility of modern 4DCT imaging systems in guiding cardiac resynchronization therapy (CRT).

4.1 | Limitations

The methods described in this study could be expanded to measure sensitivity to motion artifacts on the entire 3D endocardium. In the current form, 1 cm thick axial slabs of the phantom’s endocardial surface were extracted; since these slabs were fixed in space, there was movement of phantom tissue into and out of the imaging plane as the phantom was programmed to contract and relax. Motion correction was then performed on the images of these axial slabs. As the motion of the human heart is highly 3D in nature, future studies investigating the accuracy and precision of measuring mechanical activation times of the entire 3D endocardium could be performed.

Low X-ray dosage implies low image quality. The images of the 3D printed phantom cylinders were acquired under 350 mA and 100 kVp tube current settings, which constitutes a “medium” dose scan. While this study succeeded in demonstrating the high accuracy and precision of estimating mechanical activation times from 4DCT images with ResyncCT motion correction, the effect of dose on the accuracy and precision of those estimates should be investigated.

The dyssynchronous phantom developed in this study utilized a set of displacements that yielded endocardial strains typical of those observed in a patient with an LBBB or RV apical pacing.^{23,24} While the designed strain functions were sufficient to demonstrate the potential value of 4DCT + ResyncCT in the estimation of mechanical activation times of LV wall motion, future studies could explore the effect of varying regional and global LV function. Additionally, the strain functions were smooth in nature with a linear interpolation of strains between the delayed lateral wall and the earlier activating septum. While the highly detailed motions of hearts may contain fast subtle motions, the programmed motion of the phantom was sufficient to accurately model the “stationary-wall” and the “double-wall” artifacts, which are the primary sources of error when estimating mechanical activation times of the myocardial walls with 4DCT.

The dynamics of endocardial boundary motion during systole were investigated using two m-mode lines, one on the lateral wall and the other on the septum. Both m-mode lines sampled endocardial wall motion in phase with different gantry angles during data acquisition. While sampling endocardial wall motion at only two locations is a limitation, we believe this limited spatial sampling is compensated for by simulating five

different starting gantry angles. The starting gantry angles were simulated in increments of 45°; this effectively led to sampling locations on the endocardium by m-mode lines perpendicular to the surface rotating in 45° increments.

As shown from phantom experiments in this study, 4DCT + ResyncCT yielded highly accurate estimates of mechanical activation times of endocardial wall motion. The promising initial results reported in this work motivate future studies to perform head-to-head validation in patients against CMR tagging, the gold-standard modality for estimating regional cardiac function.

5 | CONCLUSIONS

We developed an anthropomorphically accurate dyssynchronous LV phantom and used this phantom to evaluate the accuracy and precision of estimating mechanical activation times of LV wall motion with 4DCT. After motion correction with the ResyncCT algorithm, 4DCT yields estimates of mechanical activation times of LV wall motion with significantly improved accuracy and precision. The promising results reported in this study highlight the potential utility of 4DCT in measuring the timing of mechanical events of interest for CRT guidance.

ACKNOWLEDGEMENTS

This study was supported by the NHLBI of the National Institutes of Health under award number R01 HL144678 (McVeigh). The content is solely the responsibility of the authors and does not necessarily represent the official views of the National Institutes of Health. This work was done during the term of an Award from the American Heart Association (AHA 20PRE35210261).

CONFLICT OF INTEREST

Dr. McVeigh holds founder shares in Clearpoint Neuro Inc. and receives research funding from GE Healthcare, Abbott Medical, and Pacesetter Inc.

REFERENCES

- Rybicki FJ, Otero HJ, Steigner ML, et al. Initial evaluation of coronary images from 320-detector row computed tomography. *Int J Cardiovasc Imaging*. 2008;24(5):535-546.
- Kitagawa K, Lardo AC, Lima JAC, George RT. Prospective ECG-gated 320 row detector computed tomography: implications for CT angiography and perfusion imaging. *Int J Cardiovasc Imaging*. 2009;25(S2):201-208.
- Schuleri KH, George RT, Lardo AC. Applications of cardiac multidetector CT beyond coronary angiography. *Nat Rev Cardiol*. 2009;6(11):699-710.
- Cruz-Bastida JP, Gomez-Cardona D, Li K, et al. Hi-Res scan mode in clinical MDCT systems: experimental assessment of spatial resolution performance. *Med Phys*. 2016;43(5):2399-2409.
- Pourmorteza A, Schuleri KH, Herzka DA, Lardo AC, McVeigh ER. A new method for cardiac computed tomography regional function assessment. *Circ Cardiovasc Imaging*. 2012;5(2):243-250.
- Manohar A, Rossini L, Colvert G, et al. Regional dynamics of fractional dimension of the left ventricular endocardium from cine computed tomography images. *J Med Imaging*. 2019;6(04):1.
- Vernooy K, van Deursen CJM, Strik M, Prinzen FW. Strategies to improve cardiac resynchronization therapy. *Nat Rev Cardiol*. 2014;11(8):481-493.
- Mirea O, Pagourelas ED, Duchenne J, et al. Variability and reproducibility of segmental longitudinal strain measurement. *JACC Cardiovasc Imaging*. 2018;11(1):15-24.
- Mirea O, Pagourelas ED, Duchenne J, et al. Intervendor differences in the accuracy of detecting regional functional abnormalities. *JACC Cardiovasc Imaging*. 2018;11(1):25-34.
- Daubert J-C, Saxon L, Adamson PB, et al. EHRA/HRS expert consensus statement on cardiac resynchronization therapy in heart failure: implant and follow-up recommendations and management: a registered branch of the European Society of Cardiology (ESC), and the Heart Rhythm Society; and in col. *Europace*. 2012;14(9):1236-1286.
- Truong QA, Singh JP, Cannon CP, et al. Quantitative analysis of intraventricular dyssynchrony using wall thickness by multidetector computed tomography. *JACC Cardiovasc Imaging*. 2008;1(6):772-781.
- Truong QA, Szymonifka J, Picard MH, et al. Utility of dual-source computed tomography in cardiac resynchronization therapy—DIRECT study. *Heart Rhythm*. 2018;15(8):1206-1213.
- Behar JM, Rajani R, Pourmorteza A, et al. Comprehensive use of cardiac computed tomography to guide left ventricular lead placement in cardiac resynchronization therapy. *Heart Rhythm*. 2017;14(9):1364-1372.
- Kidoh M, Shen Z, Suzuki Y, et al. False dyssynchrony: problem with image-based cardiac functional analysis using X-ray computed tomography. In: Flohr TG, Lo JY, Gilat Schmidt T, eds. *Medical Imaging 2017: Physics of Medical Imaging*. 2017:101321U. <https://doi.org/10.1117/12.2250257>
- Contijoch F, Stayman JW, McVeigh ER. The impact of small motion on the visualization of coronary vessels and lesions in cardiac CT: a simulation study. *Med Phys*. 2017;44(7):3512-3524.
- Li Y, Cao X, Xing Z, Sun X, Hsieh J, Chen G-H. Image quality improvement in MDCT cardiac imaging via SMART-RECON method. In: Flohr TG, Lo JY, Gilat Schmidt T, eds. *Medical Imaging 2017: Physics of Medical Imaging*. SPIE 10132; 2017:101322Z.
- Auger DA, Bilchick KC, Gonzalez JA, et al. Imaging left-ventricular mechanical activation in heart failure patients using cine DENSE MRI: validation and implications for cardiac resynchronization therapy. *J Magn Reson Imaging*. 2017;46(3):887-896.
- Gao X, Abdi M, Auger DA, et al. Cardiac magnetic resonance assessment of response to cardiac resynchronization therapy and programming strategies. *JACC Cardiovasc Imaging*. 2021;14:2369-2383.
- Wyman BT, Hunter WC, Prinzen FW, McVeigh ER. Mapping propagation of mechanical activation in the paced heart with MRI tagging. *Am J Physiol Circ Physiol*. 1999;276(3):H881-H891.
- Faris OP, Evans FJ, Ennis DB, et al. Novel technique for cardiac electromechanical mapping with magnetic resonance imaging tagging and an epicardial electrode sock. *Ann Biomed Eng*. 2003;31(4):430-440.
- Manohar A, Colvert GM, Schluchter A, Contijoch F, McVeigh ER. Anthropomorphic left ventricular mesh phantom: a framework to investigate the accuracy of SQUEEZ using Coherent Point Drift for the detection of regional wall motion abnormalities. *J Med Imaging*. 2019;6(04):1.
- Yushkevich PA, Piven J, Hazlett HC, et al. User-guided 3D active contour segmentation of anatomical structures: significantly improved efficiency and reliability. *Neuroimage*. 2006;31(3):1116-1128.
- Helm RH, Leclercq C, Faris OP, et al. Cardiac dyssynchrony analysis using circumferential versus longitudinal strain. *Circulation*. 2005;111(21):2760-2767.

24. Delgado V, Ypenburg C, van Bommel RJ, et al. Assessment of left ventricular dyssynchrony by speckle tracking strain imaging. *J Am Coll Cardiol*. 2008;51(20):1944-1952.
25. Lumens J, Leenders GE, Cramer MJ, et al. Mechanistic evaluation of echocardiographic dyssynchrony indexes. *Circ Cardiovasc Imaging*. 2012;5(4):491-499.
26. Pack JD, Manohar A, Ramani S, et al. Four-dimensional computed tomography of the left ventricle, Part I: motion artifact reduction. *Under Concurr Rev Med Phys*. 2021.
27. Kim S, Chang Y, Ra JB. Cardiac motion correction based on partial angle reconstructed images in X-ray CT. *Med Phys*. 2015;42(5):2560-2571.
28. Strotmann JM, Kvitting J-PE, Wilkenshoff UM, Wranne B, Hatle L, Sutherland GR. Anatomic m-mode echocardiography: a new approach to assess regional myocardial function—A comparative in vivo and in vitro study of both fundamental and second harmonic imaging modes. *J Am Soc Echocardiogr*. 1999;12(5):300-307.
29. Feigenbaum H. Role of m-mode technique in today's echocardiography. *J Am Soc Echocardiogr*. 2010;23(3):240-257.
30. Otsu N. A threshold selection method from gray-level histograms. *IEEE Trans Syst Man Cybern*. 1979;9(1):62-66.
31. Cheung AA, Niu Tianye, Faber TL, Segars WP, Zhu Lei & Chen Ji. Simulation of left ventricular dyssynchrony using the XCAT phantom. In: IEEE Nuclear Science Symposium and Medical Imaging Conference. IEEE; 2010:3187-3189.
32. Zwanenburg JJM, Götte MJW, Kuijjer JPA, Heethaar RM, van Rossum AC, Marcus JT. Timing of cardiac contraction in humans mapped by high-temporal-resolution MRI tagging: early onset and late peak of shortening in lateral wall. *Am J Physiol Circ Physiol*. 2004;286(5):H1872-H1880.
33. van Bommel RJ, Tanaka H, Delgado V, et al. Association of intraventricular mechanical dyssynchrony with response to cardiac resynchronization therapy in heart failure patients with a narrow QRS complex. *Eur Heart J*. 2010;31(24):3054-3062.
34. Andersson LG, Wu KC, Wieslander B, et al. Left ventricular mechanical dyssynchrony by cardiac magnetic resonance is greater in patients with strict vs nonstrict electrocardiogram criteria for left bundle-branch block. *Am Heart J*. 2013;165(6):956-963.
35. Bader H, Garrigue S, Lafitte S, et al. Intraleft ventricular electromechanical asynchrony. *J Am Coll Cardiol*. 2004;43(2):248-256.
36. Bolus NE. NCRP Report 160 and what it means for medical imaging and nuclear medicine. *J Nucl Med Technol*. 2013;41(4):255-260.

SUPPORTING INFORMATION

Additional supporting information may be found in the online version of the article at the publisher's website.

How to cite this article: Manohar A, Pack JD, Schluchter AJ, McVeigh ER. Four-dimensional computed tomography of the left ventricle, Part II: estimation of mechanical activation times. *Med Phys*. 2022;1-15.
<https://doi.org/10.1002/mp.15550>